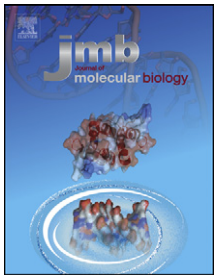

In Silico Derived Small Molecules Bind the Filovirus VP35 Protein and Inhibit Its Polymerase Cofactor Activity

Craig S. Brown[1,2,3,†], Michael S. Lee[4,5,†], Daisy W. Leung[1,†], Tianjiao Wang[2], Wei Xu[1], Priya Luthra[6], Manu Anantpadma[7], Reed S. Shabman[6], Lisa M. Melito[8], Karen S. MacMillan[8], Dominika M. Borek[8,9,10], Zbyszek Otwinowski[8,9,10], Parameshwaran Ramanan[1,11], Alisha J. Stubbs[2,3], Dayna S. Peterson[2,3], Jennifer M. Binning[1,11], Marco Tonelli[12], Mark A. Olson[5], Robert A. Davey[7], Joseph M. Ready[8], Christopher F. Basler[6] and Gaya K. Amarasinghe[1]

1 - Department of Pathology and Immunology, *Washington University School of Medicine, St. Louis, MO 63110, USA*
2 - Roy J. Carver Department of Biochemistry, *Biophysics and Molecular Biology, Iowa State University, Ames, IA 50011, USA*
3 - Biochemistry Undergraduate Program, *Iowa State University, Ames, IA 50011, USA*
4 - Simulation Sciences Branch, *US Army Research Laboratory, Aberdeen, MD 21005, USA*
5 - Department of Cell Biology and Biochemistry, *USAMRIID, 1425 Porter St., Fort Detrick, MD 21702, USA*
6 - Department of Microbiology, *Icahn School of Medicine at Mount Sinai, New York, NY 10029, USA*
7 - Department of Virology and Immunology, *Texas Biomedical Research Institute, San Antonio, TX 78227, USA*
8 - Department of Biochemistry, *UT Southwestern Medical Center at Dallas, Dallas, TX 75390, USA*
9 - Department of Biophysics, *UT Southwestern Medical Center at Dallas, Dallas, TX 75390, USA*
10 - Center for Structural Genomics of Infectious Diseases (CSGID), *Chicago, IL, USA*
11 - Biochemistry Graduate Program, *Iowa State University, Ames, IA 50011, USA*
12 - National Magnetic Resonance Facility at Madison, *University of Wisconsin, Madison, 433 Babcock Drive, Madison, WI 53706, USA*

Correspondence to Gaya K. Amarasinghe: *gamarasinghe@path.wustl.edu*
http://dx.doi.org/10.1016/j.jmb.2014.01.010
Edited by M. F. Summers

Abstract

The Ebola virus (EBOV) genome only encodes a single viral polypeptide with enzymatic activity, the viral large (L) RNA-dependent RNA polymerase protein. However, currently, there is limited information about the L protein, which has hampered the development of antivirals. Therefore, antifiloviral therapeutic efforts must include additional targets such as protein–protein interfaces. Viral protein 35 (VP35) is multifunctional and plays important roles in viral pathogenesis, including viral mRNA synthesis and replication of the negative-sense RNA viral genome. Previous studies revealed that mutation of key basic residues within the VP35 interferon inhibitory domain (IID) results in significant EBOV attenuation, both *in vitro* and *in vivo*. In the current study, we use an experimental pipeline that includes structure-based *in silico* screening and biochemical and structural characterization, along with medicinal chemistry, to identify and characterize small molecules that target a binding pocket within VP35. NMR mapping experiments and high-resolution x-ray crystal structures show that select small molecules bind to a region of VP35 IID that is important for replication complex formation through interactions with the viral nucleoprotein (NP). We also tested select compounds for their ability to inhibit VP35 IID–NP interactions *in vitro* as well as VP35 function in a minigenome assay and EBOV replication. These results confirm the ability of compounds identified in this study to inhibit VP35–NP interactions *in vitro* and to impair viral replication in cell-based assays. These studies provide an initial framework to guide development of antifiloviral compounds against filoviral VP35 proteins.

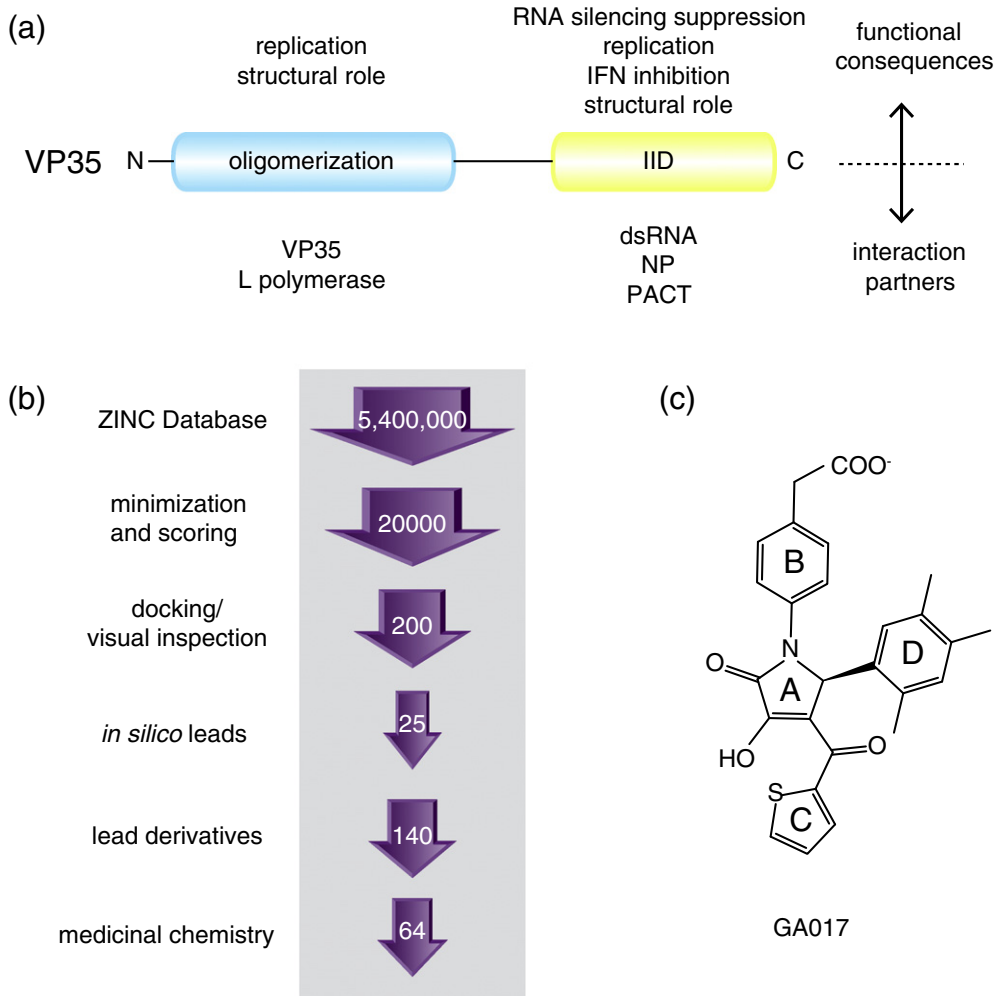

Fig. 1. Filoviral VP35 proteins are multifunctional targets for therapeutic development. (a) Domain organization of filoviral VP35 based on previous biochemical and structural studies [12]. Approximately 140 amino acids at the N-terminus form the oligomerization domain and the 125 C-terminal amino acids form the IID. The different interaction partners for both domains and the corresponding functional consequences are listed. (b) Outline of the structure-based *in silico* screening approach used in this study. The number of compounds screened at each stage is indicated within the arrows. Experimental screening included 25 initial compounds, followed by 140 GA-series analogs, and 64 optimized compounds (VPL) synthesized using binding and structural data obtained from the GA-series molecules. (c) The chemical structure of GA017 containing the pyrrolidinone scaffold.

Introduction

Ebola virus (EBOV) and Marburg virus (MARV) are members of the *Filoviridae* family of single-stranded, nonsegmented negative-sense RNA viruses. EBOV and MARV infections are characterized by severe hemorrhagic fever, which have led to fatality rates nearing 90% in some outbreaks [1]. The virulence of filoviruses makes antifiloviral therapeutics a priority. However, these viruses encode only one protein, large protein (L), which exhibits enzymatic activity. Therefore, efforts to target nonenzymatic viral proteins with small molecules are an important antiviral development strategy. However, targeting nonenzymatic proteins at protein–protein interfaces (PPIs) is challenging and often requires detailed structural and functional information about protein–protein complexes and interfaces. Unlike enzymatic active sites, PPIs are often shallow with limited molecular features that can facilitate ligand binding.

High fatality rates have been attributed, in part, to the ability of EBOV and MARV to efficiently subvert host innate immune responses as well as subsequent adaptive immune responses [1–3]. Among the strategies employed are suppression of interferon (IFN)-α/β production and inhibition

of IFN-α/β-induced antiviral signaling [4–9]. Of particular note, the suppression of IFN-α/β responses is critical for EBOV virulence [10,11]. Use of multiple strategies for immune suppression by filoviruses underscores the importance of targeting conserved viral factors.

The filoviral viral protein 35 (VP35) is an attractive potential therapeutic target because it carries out multiple functions critical for viral replication and its C terminal domain structure is known to high resolution. It is an important multifunctional protein that can antagonize host immune responses, including IFN production initiated by retinoic-acid-inducible gene-I-like receptors (RLRs), and it functions as a cofactor in the viral polymerase complex (Fig. 1a). VP35 consists of an N-terminal coiled-coil domain [13] and a C-terminal domain termed the IFN inhibitory domain (IID) [14–18]. In the IID, there are two basic patches: the first basic patch (FBP) is important for interactions with EBOV nucleoprotein (NP) and VP35 polymerase cofactor function and the central basic patch (CBP) is important for VP35 dsRNA binding and IFN inhibition [17,18] (Supplementary Fig. 1). Recombinant viruses with VP35 mutations are greatly attenuated in guinea pigs and protect against subsequent EBOV infection [11]. In addition, RNAi against VP35 also attenuated viral growth [19]. Together, these observations support the therapeutic potential of VP35 [11]. The availability of high-resolution structures of the VP35 IID domains of EBOV Zaire (eIID) [17], Reston (rIID) [18,20], and MARV (mIID) [21] provides a new opportunity for structure-based antiviral development [22].

Here, we describe studies that identify, validate, and functionally characterize small-molecule binders that target a key PPI between VP35 and NP. To this end, we employed an *in silico* screen using the structure of the Zaire EBOV VP35 IID (eIID) as a target for efficient and cost-effective lead identification. In the current study, we use an experimental pipeline that includes structure-based *in silico* screening and biochemical and structural characterization along with medicinal chemistry to identify and characterize small molecules that target a key binding pocket within VP35. High-resolution structural studies and NMR mapping experiments show that select small molecules bind within the region of VP35 that is important for interaction with the viral NP and replication complex formation. We also tested select compounds for their ability to inhibit VP35–NP interactions *in vitro*, to inhibit VP35 function in a cell-based minigenome (MG) assay, and to inhibit EBOV replication. Altogether, these studies show that small molecules identified through an *in silico* screen can bind filoviral VP35 proteins and inhibit its replication function. Our studies also provide a framework to guide development of antifiloviral compounds against VP35 proteins.

Results

In silico screening

A total of 5.4 million drug-like small molecules from the ZINC library [23] were docked to the eIID [Protein Data Bank (PDB) ID: 3FKE] and the top *in silico* hits were validated by an NMR-based assay (Fig. 1). Two hundred compounds were selected after the final screening and docked models were subjected to visual inspection and selection. Of these, 25 compounds were subsequently selected for NMR-based binding studies. Compounds used for *in vitro* validation were selected based on LigScores of 5.5–6.5 and Log*P* values <5. Of the 25 compounds tested, we identified 5 compounds with dissociation constant (K_d) values of 550–1278 μM (Fig. 2a; Supplementary Table 1). All five compounds contained common structural elements and are represented by GA017 with a pyrrolidinone

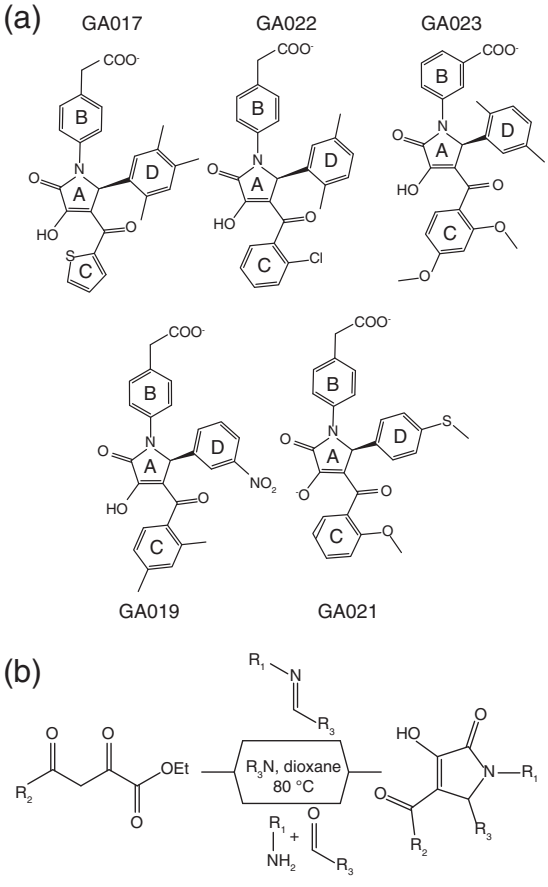

Fig. 2. Chemical structures of representative compounds that bind VP35 IID. (a) Compounds with methyl substitutions in the phenyl D-ring bind with higher affinity compared to nucleophilic substitutions. (b) Outline of the chemical synthesis scheme to generate pyrrole-based compounds.

scaffold (Fig. 1c). In order to optimize binding, we identified additional compounds that contained the pyrrolidinone scaffold of GA017 through structural interaction fingerprint analysis [24], and these were either purchased or synthesized (complete results of the chemical synthesis process, including NMR validation, are described in Supplementary Materials and Methods). *In silico* findings were validated by a series of biochemical, structural, and functional characterizations of VP35–compound interactions (Fig. 1b). Overall, these efforts resulted in an 18-fold enhancement in binding affinity.

Compounds containing pyrrolidinone scaffold bind eIID

NMR-based binding studies revealed that eIID–compound interactions occur in the fast-exchange regime relative to the chemical shift time scale as judged by the full titration data for GA017 (Fig. 3, Supplementary Fig. 2). Of note, while most compound binding resulted in linear chemical shift changes upon titration, indicative of a single free and bound conformation, there were several peaks that deviated. While the exact cause of this deviation is unknown, we suspect that a combination of the influence of the small-molecule chemistry and exchange regime of binding are likely contributors to this phenomenon. Therefore, $^{1}H–^{15}N$ heteronuclear single quantum coherence (HSQC) titration data from only residues that displayed linear peak migration patterns between a single free and bound state were used to determine the binding affinity. We were able to extract dissociation constants using two methods by plotting the normalized change in chemical shift *versus* concentration. We carried out titrations between 0

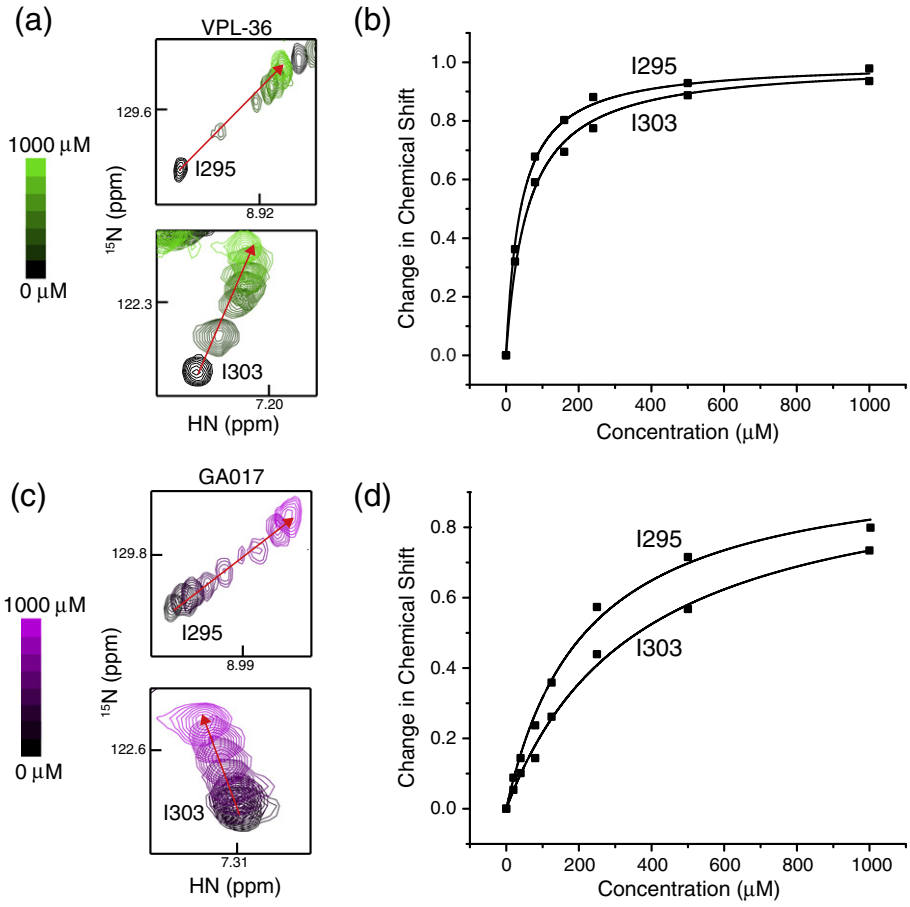

Fig. 3. NMR-based studies reveal SAR for pyrrolidinone scaffold containing ligands that bind with high affinity to the first basic patch of VP35 IID. Titration of VPL36 (green) or GA017 (purple) into ^{15}N-labeled eIID resulted in a large number of chemical shift perturbations. (a) VPL36 titration monitored at residues Ile295 and Ile303. (b) Plot of normalized chemical shift change *versus* compound concentration for two residues, Ile295 and I303, when VPL36 is titrated into ^{15}N-labeled eIID. (c) GA017 titration as monitored at residues Ile295 and Ile303. (d) Plot of normalized chemical shift change *versus* concentration for two residues, Ile295 and I303, when GA017 is titrated into ^{15}N-labeled eIID. Dissociation constants were measured by fitting average chemical shift deviation (see Materials and Methods) at each concentration of titrant.

and 1000 μM for select compounds and K_d values were calculated using the chemical shifts of two to three residues (Fig. 3). Among these, Ile303 on VP35 IID was the best reporter of small-molecule binding, due to the large chemical shift difference between free and bound form as well as proximity to the binding site. Therefore, the estimate of dissociation constants for each small molecule was determined using the chemical shift differences derived from the averaged titration curves using Ile303 (Supplementary Fig. 3). Following this method, we tested 146 compounds, termed the GA series, obtained through a commercial vendor (Enamine Inc., Kiev, Ukraine), and an additional 64 compounds, termed the VPL series, which were synthesized at UT Southwestern Medical Center at Dallas (Fig. 2b and Supplementary Materials and Methods). Structures and the estimated binding affinities defined through our NMR-based binding assay are reported in Supplementary Table 1 (arranged by potency) and in Supplementary Table 2 (arranged by functional groups). These results indicate that we have compounds with an estimated K_d range from ~30 μM to ~10 mM and have at least one compound containing the pyrrolidinone scaffold with no observable binding (VPL64). A summary of our structure activity relationships, shown in Fig. 4, reveals a number of important trends that provide insight into eIID–compound interactions. For example, binding requires a *meta*-CH_2CO_2H or a *para*-CH_2-CO_2H in the B-ring (Supplementary Table 2) and a thiophene or a substituted phenyl group at the C-ring. In contrast, a number of different aromatic groups can be accommodated at the D-ring. Interestingly, the largest variations in binding affinities are due to changes in the D-ring (Supplementary Table 2). For example, replacing a phenyl D-ring with a thiophenyl ring containing a halogen atom, such as Cl or Br as a substituent, results in over 10-fold K_d enhancement. Substituting this thiophenyl ring for other substituents, or even removing the halogen atom alone results in a 10-fold higher K_d (see GA229 *versus* VPL36), which further highlights the importance of this interaction. Chemical groups that enhance binding at the D-ring are interchangeable with the C-ring. A *meta*-trifluoromethyl group present in several of the tightest binding compounds at the D-ring shows high-affinity binding when present at both the C- and D-ring positions (e.g., VPL58). Finally, compounds lacking an aromatic group at the C-ring or containing large chemical groups at the B-, C-, or D-rings displayed near loss of binding (e.g., VPL56, VPL62, GA017-F2, and GA219).

Compounds bind near the eIID first basic patch

In order to structurally characterize eIID–compound interactions, we generated co-crystal structures of select compounds by soaking native eIID crystals (Table 1). Consistent with our docking predictions (data not shown) and NMR chemical shift mapping (discussed above), all pyrrolidinone compounds bind near a pocket formed by residues from the α-helical and β-sheet subdomains, including Ala221, Arg225, Gln241, Leu242, Lys248, Lys251, Pro293, Ile295, Ile297, Asp302, and Phe328 (Fig. 5a and b). In all, about 20 residues from the eIID protein make up the pocket. Correspondingly, more than 50% of accessible surface area of all compounds is buried

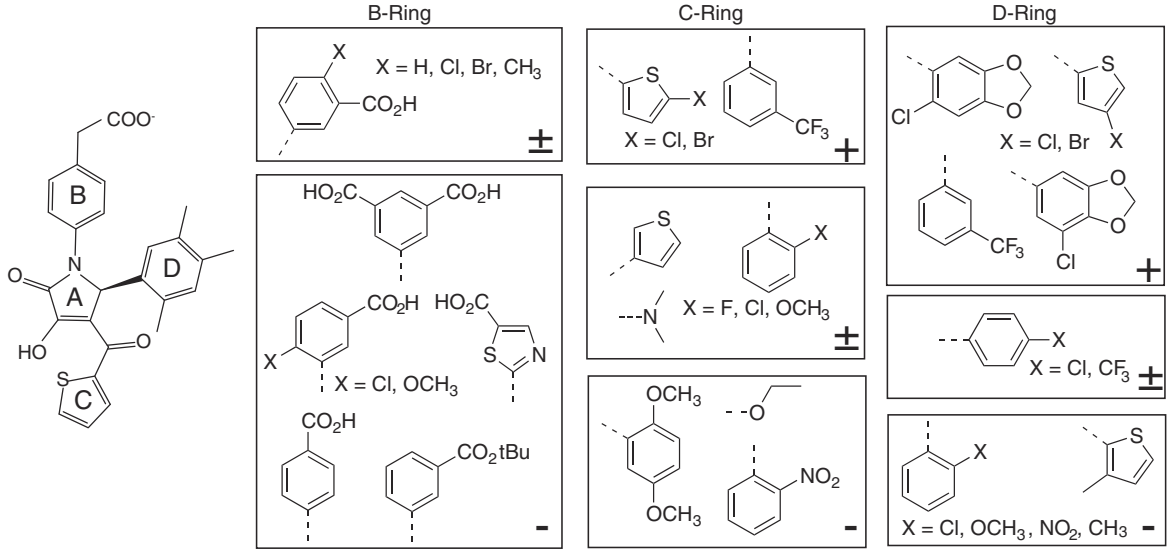

Fig. 4. Summary of key functional groups that impact ligand binding to eIID. The relative impact of functional groups are represented with respect to either GA017 or a closely related compound and the ranking is indicated by +, ±, and – for enhanced binding, no impact, and diminished binding, respectively.

Table 1. Data collection, structure solution, and refinement statistics

	VP35 IID–GA017	VP35 IID–GA246	VP35 IID–VPL27	VP35 IID–VPL29	VP35	VP35 IID–VPL48	VP35 IID–VPL51	VP35 IID–VPL57	VP35 IID–VPL58	VP35 IID–VPL60
	4IBB	4IBC	4IBD	4IBE	4IBF	4IBG	4IBH	4IBI	4IBJ	4IBK
Data collection										
Space group	$P2_12_12_1$	$P2_12_12_1$	$P2_12_12_1$	$P2_12_12_1$	$P2_12_12_1$	$P2_12_12_1$	$P2_12_12_1$	$P2_12_12_1$	$P2_12_12_1$	$P2_12_12_1$
Unit cell parameters										
a, *b*, *c* (Å)	51.47, 65.78, 72.22	51.95, 65.90, 72.04	51.56, 65.49, 72.60	51.57, 65.51, 72.16	51.47, 65.95, 72.00	51.47, 65.94, 72.48	51.38, 65.80, 72.79	51.30, 65.45, 72.65	51.26, 66.35, 72.66	51.22, 65.69, 72.83
Resolution range (Å)	40.00–1.75 (1.78–1.75)	50.00–1.74 (1.77–1.74)	50.00–1.84 (1.87–1.84)	50.00–1.95 (1.98–1.95)	50.00–2.29 (2.33–2.29)	50.00–1.41 (1.43–1.41)	50.00–1.88 (1.91–1.88)	50.00–1.46 (1.49–1.46)	50.00–1.54 (1.57–1.54)	50.00–1.85 (1.88–1.85)
Unique reflections	24,103	25,426	21,924	17,475	11,548	47,377	20,598	40,626	36,721	21,610
Redundancy	5.2 (4.1)	6.4 (3.9)	8.4 (7.3)	4.4 (3.3)	6.9 (7.2)	7.6 (2.1)	7.3 (5.8)	7.9 (4.7)	6.7 (5.1)	6.9 (5.6)
Completeness (%)	95.3 (83.3)	98.7 (90.3)	99.8 (96.8)	93.6(94.5)	99.9 (100.0)	98.8 (87.3)	99.9 (100.0)	93.9 (33.3)	98.1 (83.1)	99.9 (99.5)
R_{merge} (%)	11.2 (46.1)	12.5 (69.6)	11.7 (92.7)	11.5 (86.2)	12.1 (50.3)	10.0 (74.0)	14.8 (95.9)	8.0 (54.1)	8.2 (65.2)	12.5 (48.1)
$\langle I \rangle / \langle \sigma \rangle$	15.4 (1.7)	23.7 (2.1)	23.9 (2.0)	12.7 (2.1)	15.6 (4.3)	30.8 (2.1)	20.4 (2.3)	32.8 (1.9)	22.6 (2.3)	31.2 (6.3)
Structure solution and refinement										
Resolution (Å)	35.11–1.75 (1.80–1.75)	32.95–1.74 (1.81–1.74)	35.38–1.84 (1.92–1.84)	48.50–1.94 (2.00–1.94)	40.58–2.29 (2.52–2.29)	31.76–1.41 (1.44–1.41)	29.98–1.88 (1.98–1.88)	41.91–1.47 (1.51–1.47)	35.42–1.54 (1.56–1.54)	41.90–1.85 (1.93–1.85)
No. of reflections	21,174	25,243	21,830	15,087	10,367	47,217	20,156	40,482	31,662	21,347
Completeness (%)	83.7 (55.0)	97.8 (88.0)	99.3 (95.0)	80.2 (40.0)	89.9 (67.0)	98.5 (85.0)	97.6 (95.0)	96.3 (76.0)	84.7 (41.0)	98.7 (97.0)
Non-hydrogen atoms	2141	2163	2206	2104	2068	2205	2154	2201	2259	2234
R_{work}/R_{free} (%)	18.1/22.7	19.0/25.0	17.7/23.3	18.3/23.3	18.0/26.0	17.8/20.0	18.1/22.7	19.0/23.7	18.3/22.9	19.3/24.1
rmsd										
Bond lengths (Å)	0.006	0.006	0.007	0.006	0.008	0.007	0.007	0.007	0.006	0.007
Bond angles (°)	1.05	1.025	1.239	1.200	1.145	1.162	1.218	1.346	1.092	1.183
B-factors (Å^2)										
Protein										
Chain A	23.8	23.8	20.3	30.0	35.8	15.9	18.0	21.5	21.2	17.5
Chain B	23.8	22.7	18.8	27.5	38.8	15.5	17.7	22.0	21.2	17.2
Small molecule										
Chain C	38.6	40.2	23.4	32.4	46.3	17.2	22.7	20.1	25.7	21.0
Chain D	36.4	40.1	23.4	33.2	48.4	16.3	26.0	24.4	28.0	23.0
Water	29.7	31.4	42.3	34.1	41.3	29.5	25.4	31.6	33.3	28.0
Ramachandran plot outliers (%)	0	0	0.4	0	0	0.8	0.4	0.8	0	0
MolProbity score	1.60	1.30	1.36	1.37	1.30	1.24	1.27	1.31	1.56	1.20
MolProbity clash score	4.43	5.48	6.53	6.67	5.59	4.63	5.16	5.73	11.15	4.22

Values in parentheses are for the highest-resolution shell.

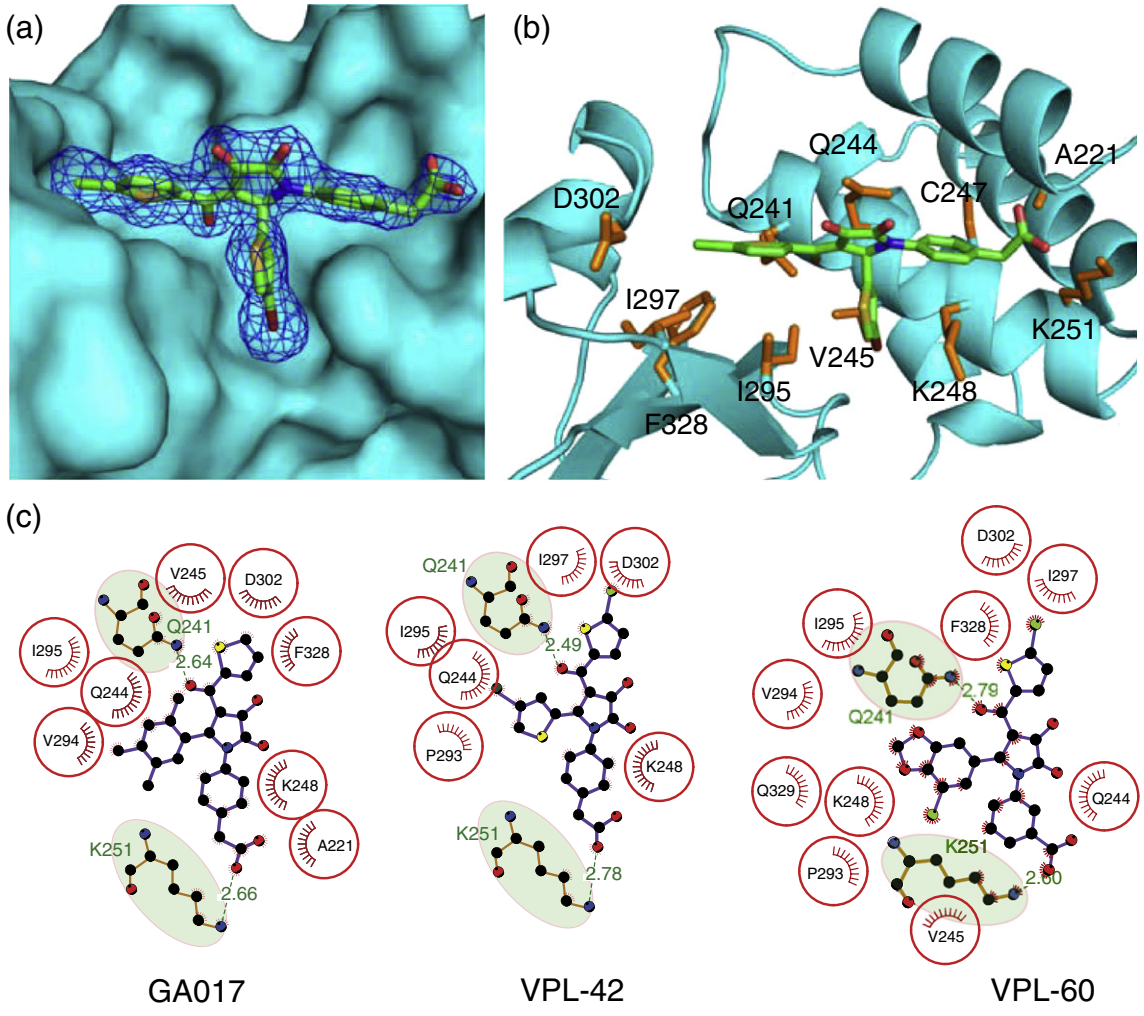

Fig. 5. *N*-aryl pyrrole-containing compounds make substantial contacts with VP35 IID near the first basic patch. Structure of eIID bound to the VPL compound is shown in (a) surface representation (cyan) with a 1σ electron density (σ_A-weighted $2F_o - F_c$) mesh for small molecules (VPL42, PDB ID: 4IBG). (b) Residue-specific contacts between eIID and VPL42 are highlighted by the amino acid side chains (orange) within 5 Å of the small molecule. (c) LigPlots showing key hydrophobic and hydrogen-bonding contacts for GA017 (PDB ID: 4IBB), VPL42 (PDB ID: 4IBG), and VPL60 (PDB ID: 4IBK).

at the VP35–NP interface in our structures. These 20 residues are distributed evenly between the α-helical and β-sheet subdomains. LigPlot [25] analysis of the eIID bound structures of GA017, VPL42, and VPL60 (Fig. 5c) shows that highly conserved hydrophobic residues, including Val245, Ile295, and Phe328, form critical interactions with the compounds. The most expansive hydrophobic interactions are with the D-ring (Fig. 5c). In addition to these common interactions, all compounds show at least two hydrogen bonds between the compound and eIID, including H-bonds with Lys251 and Gln241, which contribute to the binding energy. Removal of either the carboxylic acid or ketone moieties of the ligands completely eliminates binding based on our chemical-shift-based binding assay. Interestingly, Lys251 is important for the VP35 polymerase cofactor function, as mutations at Lys251 lead to loss of function [26]. Although most compound atoms make contact with eIID, notable absences include the hydroxyl and ketone groups from the A-ring of the pyrrolidinone scaffold, which were solvent exposed (Fig. 5). Comparison of individual compound bound structures with their respective *in silico* predictions displayed remarkable similarity in the location and local contacts by the compounds (Supplementary Fig. 4). Further confirmation of compound binding was carried out with the use of two IID mutants, Lys248A and Ile295A. Mutation of these two critical residues individually resulted in near-complete loss of compound binding (Fig. 6), while residues outside the binding pocket had no impact on ligand binding. Next, we tested the ability of select compounds to bind rIID and mIID because of the high structural similarity among these IID domains and eIID. Results

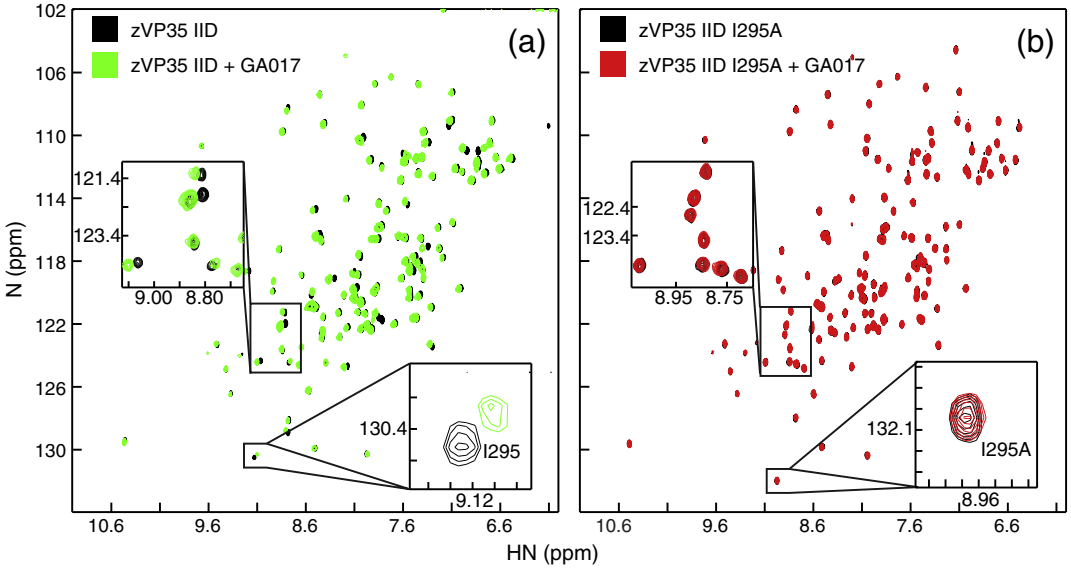

Fig. 6. Mutating residues in the binding pocket abrogate small-molecule binding. $^{1}H–^{15}N$ HSQC spectra are shown for (a) ^{15}N-enriched zVP35 IID WT in the absence (black) or presence (green) of GA017 and (b) ^{15}N-enriched eVP35 IID I295A in the absence (black) or presence (red) of GA017.

of these titrations reveal that select compounds, such as GA017, bind in a pocket in mIID and rIID similar to eIID (Fig. 7). Because complete chemical shift assignments are currently not available for rIID and mIID, we are unable to confirm the exact residues involved in the binding pocket.

Pyrrolidinone compounds disrupt PPIs *in vitro*

Given the overlap between residues important for VP35–NP binding from our previous study [26] and those observed in small molecule–VP35 IID structures (Fig. 5a), we tested the ability of select compounds to disrupt VP35–NP interaction by *in vitro* pull-down assay. As shown in Fig. 8a, select compounds that bind eVP35 IID with affinities (K_d) <100 μM can inhibit VP35–NP interaction. While it is difficult to ascertain how different compounds impact this PPI in a quantitative manner, our data suggest that affinity alone may not be the determinant driving binding as demonstrated with GA017, which is a relatively high-affinity binder that shows less inhibition than VPL42 and VPL60 (compare lanes in Fig. 8a). These observations confirm the ability of the pyrrolidinone compounds to antagonize PPIs. However, the lack of correlation between affinity and inhibitory activity of the VP35–NP interaction suggests that, as expected, interface interaction is likely a complex function of binding K_d and physicochemical properties of the ligand.

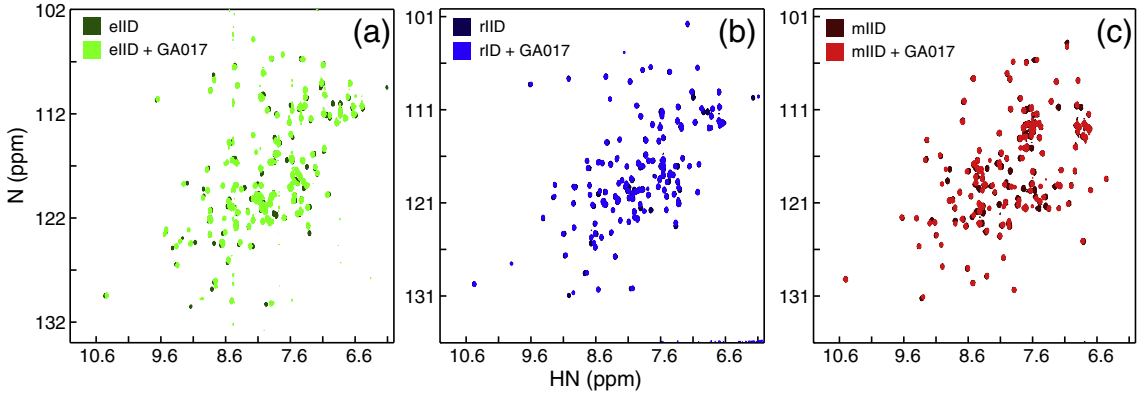

Fig. 7. *N*-aryl pyrrole-containing small molecules are panfiloviral VP35 IID binders. $^{1}H–^{15}N$ HSQC spectra of (a) eIID in the absence (dark green) or presence (light green) of GA017, (b) rIID in the absence (dark blue) or presence (light blue) of GA017, and (c) mIID in the absence (dark red) or presence (light red) of GA017.

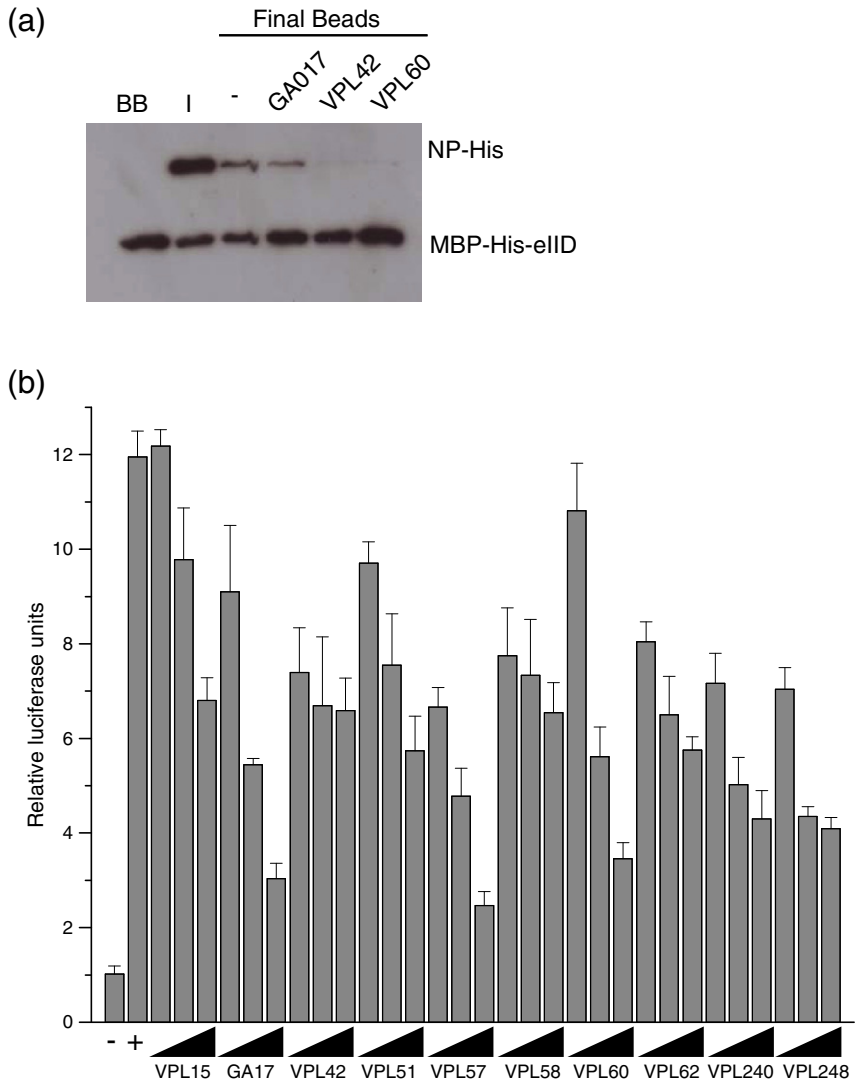

Fig. 8. Select compounds inhibit VP35–NP interaction *in vitro* and MG activity in cells. (a) Select compounds can inhibit VP35–NP interaction *in vitro* as measured by a pull-down assay. Differential levels of VP35 noted on the GA017 relative to VPL42 and VPL60 may reflect relative inhibition levels. (b) Select compounds were tested for their ability to inhibit an MG assay, and the resulting data show that some compounds do and others do not inhibit MG activity in a dose-dependent manner. Solid triangles represent 25, 50, and 100 mM concentrations of compounds as indicated in the figure. Maximum DMSO co-solvent concentration was 0.05%.

Pyrrolidinone compounds inhibit viral MG activity

Select compounds were tested for their ability to inhibit the function of the viral polymerase complex by using a previously described MG assay [26]. In this system, the viral polymerase complex is reconstituted by transfecting cells with expression plasmids for the EBOV NP, VP35, VP30, and L proteins and for a model viral genome encoding only a Renilla luciferase reporter gene. These results, shown in Fig. 8b for several compounds, including that for GA017, show that our pyrrolidinone compounds can antagonize viral MG function in a dose-dependent manner. In addition to the MG activity, we also measured the levels of firefly luciferase produced from cotransfected constitutively expressed mammalian expression plasmids. At 0, 25, 50, and 100 μM compounds, no statistical difference between relative levels of firefly luciferase activity was detected (Supplementary Fig. 5), suggesting that these compounds do not specifically influence the luciferase activity, nor do they cause significant cell toxicity.

Select compounds inhibit EBOV

Compounds were tested for their ability to inhibit a replication-competent EBOV in a cell-based assay.

This is a recombinant virus that encodes a GFP reporter but is otherwise similar to wild-type virus for infection and pathogenicity [27]. Assays were performed at BSL-4 containment. Both initial infection efficiency and virus produced from treated cells were tested (Fig. 9). As measured by GFP reporter expression, GA248, VPL42, and VPL57 each inhibited virus infection relative to the untreated [dimethyl sulfoxide (DMSO) only] control. In contrast, VPL15, which has a lower binding affinity, showed weak inhibition (Fig. 9a). VP35 is involved in virus assembly and RNA replication complex activity and so its inhibition may have a greater impact on late stages of the replication cycle. Supernatants from BSRT7 cells infected at 0.05 MOI (multiplicity of infection) for 48 h were collected and used to infect a new monolayer of BSRT7 cells to measure this effect. For this assay, VPL42 and VPL57 were still active but now GA17, GA240, VPL60, VPL51, and VPL58 also showed strong inhibition of virus production. Again, each was more active than VPL15, but even VPL15 showed some activity (50% inhibition compared to control). This inhibition suggests that despite the lack of biochemical evidence for a strong interaction with VP35, in cells, the compound can still interfere with virus replication. However, it is unclear if this is due to a direct effect on viral VP35 protein. Interestingly, GA248, which inhibited virus infection in the GFP reporter assay, did not inhibit infectious virus release. This suggests that it may preferentially affect VP35 during an early phase of replication.

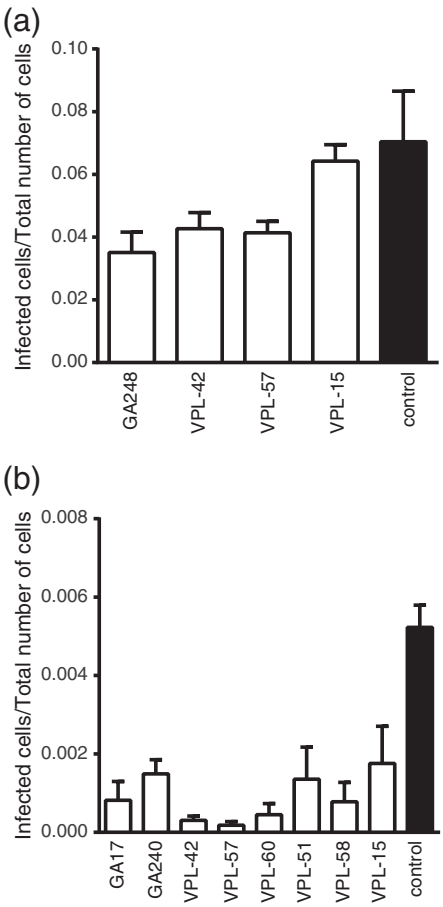

Fig. 9. Select compounds inhibit EBOV replication and release. (a) Inhibition of viral replication was monitored by the infection efficiency, which was calculated by dividing the number of infected, GFP-expressing cells by the total number of cells at 48 h post-challenge with EBOV-GFP. BRST7 cells were treated with indicated compounds at 125 μM in triplicate. (b) Inhibition of virus release was measured by the ability of supernatant to infect fresh cells. Cells treated with the indicated compounds and challenged with virus and supernatants collected after 48 h. The supernatants from these viral-infected cells (with or without compound treatment) were diluted and a portion was transferred to fresh cells. After an additional 24 h, the fresh cells were fixed and the infection efficiency was calculated as for (a). Only those compounds showing a significant ($P < 0.05$) decrease from DMSO-treated control are shown.

Discussion

Using a computational approach, we screened over 5.4 million potential compounds and, through further computational analysis and NMR-based screening methods, we identified several compounds capable of binding VP35 IID with high affinity and specificity. Structures of several compounds in complex with VP35 IID highlight several hydrophobic interactions between compound functional groups and side chains from key residues important for VP35 function *in vivo*. Therefore, these inhibitors can potentially function as leads for development of panfiloviral therapeutics.

Targeting PPIs is a challenge for therapeutic development for several reasons, including the high-energy barrier to identify lead candidates, availability for binding interactions, and a general lack of curvature limiting the number of available binding pockets with sufficient surface area for ligand binding. In contrast, active-site analogs often serve as good starting points to inhibitor optimization for enzymatic targets. Using an *in silico* screening approach allows for rapid, highly efficient, and low-cost methods for computational determination of potential binders and, when paired with a method for structural determination, allows for the optimization of binding interactions to maximize affinity and specificity. When structural knowledge regarding PPIs is available, this can be applied as an additional filter to identify *in silico* hits likely to disrupt function.

One aspect of drug design that was not addressed in our *in silico* modeling is drug access to sites where virus replication takes place. We believe that this accounts for many of the differences seen in terms of biochemical measurement of compound affinity to VP35 and activity in the MG assay or with replicating virus. The ability of a compound to partition into

water *versus* the membranes of the cell dictates ability to access these sites and reach concentrations where it can be active. For many virus types, different stages of replication occur in membranous structures or in the aqueous phase of the cytoplasm. For filoviruses, cytoplasmic inclusion bodies serve as sites of viral RNA synthesis. This means that chemical partitioning is predicted to have a large impact on antiviral activity. The assembling virus also adds an additional layer of complexity, requiring the cooperative interaction of many structural components, including NP, VP40, and VP35. While not studied here, our observation that compounds are better able to inhibit virus production than initial infection likely reflects disruption of such assembly and will be investigated in future work.

While the functional importance of filoviral VP35 is well appreciated, there is a clear gap in utilizing that knowledge to target VP35 for antiviral inhibitor development. Using a combination of *in silico* docking, biochemical and structural characterization, and functional validation, we now provide important information required for developing therapeutics against filoviral VP35s, particularly the use of available structural and functional data to define the small-molecule binding site near the NP binding region and the ability of select small molecules to inhibit VP35–NP interaction at a PPI that is critical for replication function. Our results using dose-dependent MG analysis further supports targeting of select inhibitors to the VP35–NP PPI. Finally, the ability of select compounds to inhibit GFP-expressing EBOVs further highlights the potential utility of the compounds we have identified. However, the affinities of the compounds identified are less than optimal and efforts to optimize the chemical scaffold identified here and to identify more potent inhibitors of filoviruses are underway. In addition to providing a class of small molecules that target a PPI, this study also validates the use of *in silico* docking, where functional data can guide the selection of target sites in proteins by computational methods to provide chemical leads against PPIs of high-priority pathogens that encode few enzymatic antiviral targets.

Materials and Methods

In silico screening

Autodock 4.0 [28] automated by the DOVIS pipeline [29,30] was used to screen 5.4 million compounds from the ZINC database [23] against the first basic patch groove in the crystal structure of eVP35 IID (PDB ID: 3FKE; Supplementary Fig. 1a). Energy minimization was performed on protein–compound complexes of the 20,000 top-ranked molecules using CHARMM (v. 35b2) [31] with the MMFF force field module [32]. Minimized complexes were re-ranked by LigScore2 [33]. Visual inspection of the top 100 complexes led to the purchase of 25 compounds (Enamine Inc.). One hundred thirty more compounds that had the most similar structural interacting fingerprints [24] to those hits were also selected and purchased.

Protein expression, purification, and crystallization

eVP35 IID proteins were purified as described previously [17,18,34]. Crystallization screens (Hampton Research) were used to identify initial conditions using purified VP35 IID protein and further optimized using in-house reagents with 10% DMSO. After 24–48 h, 0.4 μL of 20–50 mM compound in 100% DMSO was added to crystals and incubated at 25 °C for 1–24 h. Diffraction data were collected at the Advanced Photon Source Beamline 19ID (Argonne National Laboratory) at 100 K. Ligand-bound structures were solved by isomorphous replacement, using the structure of ligand-free eVP35 IID (PDB ID: 3FKE) as the search model, and refined using REFMAC5 [35] or PHENIX [36].

Optimization of initial hits and synthesis

In order to optimize key functional groups, we synthesized compounds based on initial SAR data obtained by NMR chemical shift mapping and structural data, including charge/surface complementation (detailed methods are described in the Supplementary Methods).

NMR spectroscopy

Stock solutions (50 mM) of small molecules were prepared by dissolving compounds in 100% d_6-DMSO. Samples containing 4–10 compounds were screened by NMR, and $^{1}H–^{15}N$ HSQC spectra were analyzed for changes in chemical shift. Up to 80 μM of each compound was added to 80 μM ^{15}N-labeled eVP35 IID samples in 10 mM Hepes (pH 7.0), 150 mM NaCl, 2 mM TCEP, 5% D_2O, and 5% d_6-DMSO. All experiments were acquired at 25 °C on a Bruker Avance II spectrometer operating at 700.13 MHz with 5 mm *z*-axis field gradient and inverse detection TXI ($^{1}H/^{13}C/^{15}N$) cryogenic probe, using the following parameters: 16 scans, 128 complex points (t_1), and 2048 total points (t_2). NMR data were processed using NMRPipe and NMRDraw [37]. NMR spectra were analyzed with NMRView [38].

Initial hits were identified by comparing $^{1}H–^{15}N$ eIID chemical shifts in the absence and presence of compound. Chemical shifts >5× digital resolution were considered significant. Initial hits were validated by titration studies as described below. Chemical shifts were obtained from $^{1}H–^{15}N$ HSQC experiments using the following equation:

$$\Delta\delta = \sqrt{(1H_{free} - 1H_{bound})^2 + \frac{(15N_{free} - 15N_{bound})^2}{10}}$$

Estimated binding constants (K_d, estimate, Supplementary Tables 1 and 2) were obtained by the following method. Twenty different compounds with varying affinities and the same pyrrolidinone scaffold structure were titrated in a concentration range of 0–1000 μM (5–8 data points). Using nonlinear least square fits, maximum chemical shift difference was obtained. For this analysis, only peaks that display

maximum shifts >3× digital resolution were selected. For single point estimations, residue I303 was selected based on several parameters, including proximity and response to binding as well as correlation between K_d values obtained using single point data and titrations (Supplementary Fig. 3). Moreover, I303 displayed good resolution with no chemical shift overlap. Maximum chemical shift differences, Δδ, and K_d values were obtained by fitting the following equation to the data:

$$\Delta\delta = \frac{B_{max} \times [\text{Ligand}]}{[\text{Ligand}] + K_d}$$

B_{max} values obtained by fitting were used to normalize Δδ for comparison of different residues within the same small-molecule data set. All single point titrations were carried out with 80 μM small-molecule ligand and the K_d values were estimated by the following equation:

$$K_d = \frac{B_{max} \times [\text{Ligand}]}{\Delta\delta} - [\text{Ligand}]$$

where [Ligand] was 80 μM and B_{max} was the average value of the fit parameter from the 20 titrations for I303. The use of I303 as an indicator of binding was validated through the correlation coefficient between the measured K_d obtained by I303 titrations.

Optimization of initial hits

Initial compounds containing the pyrrolidinone scaffold were purchased from Enamine, Inc. (see compounds with GA prefixes, Supplementary Tables 1 and 2). In order to optimize key functional groups, we synthesized compounds based on initial SAR data obtained by NMR chemical shift mapping and structural data, including charge/surface complementation (see Supplementary Methods for detailed synthesis of VPL compounds).

Structural studies

Commercial crystallization screens (Hampton Research) were used to identify initial conditions using purified eIID protein and further optimized using in-house reagents with 10% DMSO. These conditions defined as condition 1 [7 mg/mL protein solutions diluted 1:1 with 100 mM magnesium acetate (pH 7.5), 15% (wt/vol) polyethylene glycol 3350, and 10% (v/v) DMSO] or condition 2 [7 mg/ml protein solutions diluted 1:1 with 100 mM sodium citrate (pH 5.5), 15% (wt/vol) polyethylene glycol 3350, and 10% (v/v) DMSO] were used to obtain crystals grown at 25 °C using the hanging-drop vapor-diffusion method. After 24–48 h, 0.4 μL of 20–50 mM compound in 100% DMSO was added to drops containing single crystals and incubated at 25 °C for 1–24 h. Condition 1 was used to soak GA-series compounds and condition 2 was used to obtain complexes of VPL compounds. All crystals were back-soaked in reservoir solution containing 25% glycerol (wt/vol) and plunge frozen in liquid nitrogen. Diffraction data were collected at the Advanced Photon Source Beamline 19ID (Argonne National Laboratory) at 100 K. X-ray data were processed using HKL3000 [39]. Ligand-bound structures were solved by molecular replacement, using the structure of ligand-free eVP35 IID (PDB ID: 3FKE) as the search model, and refined using REFMAC5 [35] or PHENIX [36]. Small-molecule structures were generated by the PRODRG2 server and manually built into the complex structures using Coot [40]. Water molecules were added using Coot and the model was further refined with REFMAC5 or PHENIX. Structures were validated using MolProbity [41]. Data collection, refinement, and validation statistics for 10 structures corresponding to molecules GA017, GA246, VPL48, VPL51, VPL57, VPL60, VPL58, VPL27, VPL29, and VPL42 are shown in Table 1.

NP pull-down assay

Pull-down assays were performed in buffer containing 10 mM Hepes (pH 7.0), 150 mM NaCl, 5% DMSO, and 5 mM 2-mercaptoethanol at 25 °C. MBP-His-tagged eIID WT protein was immobilized on amylose resin, incubated with purified His-tagged NP protein, and subsequently washed. For small-molecule competition assays, 500 μM small molecules was incubated with MBP-His-tagged eIID prior to incubation with His-tagged NP. Following washout of unbound material, beads containing MBP-His-tagged eVP35 IID WT protein (or His-tagged eIID/His-tagged NP complex) were resolved on SDS-PAGE and Western blotted with mouse anti-His antibody (Santa Cruz Biotechnology), followed by horseradish-peroxidase-conjugated goat antimouse antibody (Bio-Rad). Membranes were developed using Millipore Immobilon Western Chemiluminescence horseradish peroxidase substrate and recorded on a ChemiDoc (Bio-Rad).

Ebola MG studies

MG assays were performed as previously described [26,42,43] with the following modifications. For the MG assay, the BSRT7 cells were transfected with expression plasmids for EBOV L, VP30, NP, and VP35, which reconstitute the EBOV RNA polymerase complex. Cotransfected was the MG plasmid that produces the MG RNA, which contains *cis*-acting sequences allowing its recognition by the reconstituted EBOV polymerase complex. The MG RNA encodes only a Renilla luciferase. A cotransfected RNA polymerase II-driven firefly luciferase expression plasmid served as a control for transfection efficiency and for cytotoxicity. Four hours after transfection, compounds were added, diluted in 250 μL of the media (dilutions were made for respective concentrations). Eighteen hours later, a dual luciferase assay (Promega) was performed following the manufacturer's protocols and read by a Promega plate reader. Luciferase activity was normalized to firefly luciferase for each group, with the negative control (without VP35) set to 1.

EBOV infections, replication, and release assays

For all EBOV infection assays, 3000 BSRT7 cells per well of a 384-well plate (Greiner Bio-One) were grown overnight in Dulbecco's modified Eagle's medium (HyClone) supplemented with 10% fetal bovine serum. The 80% confluent monolayer was treated with the indicated concentration of each compound for 1 h in triplicate. Cells were then transferred to the BSL-4 laboratory and infected

with EBOV-GFP at an MOI of 0.05. Infected cells were kept in a humidified CO_2 incubator for 48 h. At this time, 10 μL supernatant from each well was used to infect a fresh monolayer of BSRT7 cells seeded in 96-well plates. This gave a 10-fold dilution of drug-containing medium, which meant that all drugs would be inactive. Cells in the 384-well plate were fixed by immersing in neutral buffered formalin overnight. Ninety-six-well plates were fixed 24 h post-infection by immersing in neutral buffered formalin for 24 h. Fixed cells were washed three times with phosphate-buffered saline and nuclei stained with Hoecst-33342 (Life Technologies, 1:50,000 dilution). Cells were imaged on a Nikon Ti Eclipse microscope. Infected cells (green) and total cells (blue) were counted using CellProfiler software (Broad Institute) using customized pipelines that are available upon request to R. Davey. Data were analyzed and plotted using GraphPad Prism software.

Accession numbers

Coordinates and structure factors for small molecule–VP35 IID complexes have been deposited in the PDB under the following codes: 4IBB (GA017), 4IBC (GA246), 4IBD (VPL27), 4IBE (VPL29), 4IBF (VPL42), 4IBG (VPL48), 4IBH (VPL51), 4IBI (VPL57), 4IBJ (VPL58), and 4IBK (VPL60).

Acknowledgments

We thank Drs. S. Ginell, N. Duke, F. Rotella, K. Lazarski, and J. Lazarz at Argonne National Laboratory Structural Biology Center Beamlines (SBC). SBC is supported by the U.S. Department of Energy under contract DE-AC02-06CH11357. D.M.B. and Z.O. are supported in part by the Center for Structural Genomics of Infectious Diseases under the NIAID/NIH/DHS Contracts HHSN272200700058C and HHSN272201200026C Anderson (PI). This work is supported in part by National Institutes of Health grants (R01AI081914 to G.K.A. and R01AI059536, R56AI089547, R56AI093786, and R21AI097568 to C.F.B.), a Midwest Regional Center of Excellence Developmental Grant [U54AI057160-Virgin (PI) to G.K.A.], and the Welch Foundation (I-1612 to J.M.R.). DoD Defense Threat Reduction Agency Grant 4.10011_07_RD_B to M. A. O. This study made use of the National Magnetic Resonance Facility at Madison, which is supported by National Institutes of Health grants P41RR02301 (Biomedical Research Technology Program, National Center for Research Resources) and P41GM66326 (National Institute of General Medical Sciences). Equipment in the facility was purchased with funds from the University of Wisconsin, the National Institutes of Health (P41GM66326, P41RR02301, RR02781, and RR08438), the National Science Foundation (DMB-8415048, OIA-9977486, and BIR-9214394), and the U.S. Department of Agriculture.

Appendix A. Supplementary data

Supplementary data to this article can be found online at http://dx.doi.org/10.1016/j.jmb.2014.01.010.

Received 6 August 2013;
Received in revised form 25 January 2014;
Accepted 28 January 2014
Available online 1 February 2014

Keywords:
in silico drug discovery;
filoviral inhibitors;
antivirals;
VP35

† C.S.B., M.S.L., and D.W.L. contributed equally to this work.

Abbreviations used:
EBOV, Ebola virus; PPI, protein–protein interface; VP35, viral protein 35; IID, interferon inhibitory domain; NP, nucleoprotein; MARV, Marburg virus; IFN, interferon; PDB, Protein Data Bank; HSQC, heteronuclear single quantum coherence; GFP, green fluorescent protein; DMSO, dimethyl sulfoxide; MG, minigenome.

References

[1] Feldmann H, Geisbert TW. Ebola haemorrhagic fever. Lancet 2011;377:849–62.
[2] Bosio CM, Aman MJ, Grogan C, Hogan R, Ruthel G, Negley D, et al. Ebola and Marburg viruses replicate in monocyte-derived dendritic cells without inducing the production of cytokines and full maturation. J Infect Dis 2003;188:1630–8.
[3] Bray M, Geisbert TW. Ebola virus: the role of macrophages and dendritic cells in the pathogenesis of Ebola hemorrhagic fever. Int J Biochem Cell Biol 2005;37:1560–6.
[4] Reid SP, Leung LW, Hartman AL, Martinez O, Shaw ML, Carbonnelle C, et al. Ebola virus VP24 binds karyopherin alpha1 and blocks STAT1 nuclear accumulation. J Virol 2006;80:5156–67.
[5] Reid SP, Valmas C, Martinez O, Sanchez FM, Basler CF. Ebola virus VP24 proteins inhibit the interaction of NPI-1 subfamily karyopherin alpha proteins with activated STAT1. J Virol 2007;81:13469–77.
[6] Valmas C, Grosch MN, Schumann M, Olejnik J, Martinez O, Best SM, et al. Marburg virus evades interferon responses by a mechanism distinct from ebola virus. PLoS Pathog 2010;6:e1000721.
[7] Feng Z, Cerveny M, Yan Z, He B. The VP35 protein of Ebola virus inhibits the antiviral effect mediated by double-stranded RNA-dependent protein kinase PKR. J Virol 2007;81:182–92.
[8] Schumann M, Gantke T, Muhlberger E. Ebola virus VP35 antagonizes PKR activity through its C-terminal interferon inhibitory domain. J Virol 2009;83:8993–7.
[9] Kaletsky RL, Francica JR, Agrawal-Gamse C, Bates P. Tetherin-mediated restriction of filovirus budding is

antagonized by the Ebola glycoprotein. Proc Natl Acad Sci USA 2009;106:2886–91.
[10] Hartman AL, Dover JE, Towner JS, Nichol ST. Reverse genetic generation of recombinant Zaire Ebola viruses containing disrupted IRF-3 inhibitory domains results in attenuated virus growth in vitro and higher levels of IRF-3 activation without inhibiting viral transcription or replication. J Virol 2006;80:6430–40.
[11] Prins KC, Delpeut S, Leung DW, Reynard O, Volchkova VA, Reid SP, et al. Mutations abrogating VP35 interaction with double-stranded RNA render Ebola virus avirulent in guinea pigs. J Virol 2010;84:3004–15.
[12] Leung DW, Prins KC, Basler CF, Amarasinghe GK. Ebolavirus VP35 is a multifunctional virulence factor. Virulence 2010;1:526–31.
[13] Reid SP, Cardenas WB, Basler CF. Homo-oligomerization facilitates the interferon-antagonist activity of the ebolavirus VP35 protein. Virology 2005;341:179–89.
[14] Basler CF, Mikulasova A, Martinez-Sobrido L, Paragas J, Muhlberger E, Bray M, et al. The Ebola virus VP35 protein inhibits activation of interferon regulatory factor 3. J Virol 2003;77:7945–56.
[15] Cardenas WB, Loo YM, Gale Jr M, Hartman AL, Kimberlin CR, Martinez-Sobrido L, et al. Ebola virus VP35 protein binds double-stranded RNA and inhibits alpha/beta interferon production induced by RIG-I signaling. J Virol 2006;80:5168–78.
[16] Hartman AL, Towner JS, Nichol ST. A C-terminal basic amino acid motif of Zaire ebolavirus VP35 is essential for type I interferon antagonism and displays high identity with the RNA-binding domain of another interferon antagonist, the NS1 protein of influenza A virus. Virology 2004;328:177–84.
[17] Leung DW, Ginder ND, Fulton DB, Nix J, Basler CF, Honzatko RB, et al. Structure of the Ebola VP35 interferon inhibitory domain. Proc Natl Acad Sci USA 2009;106:411–6.
[18] Leung DW, Shabman RS, Farahbakhsh M, Prins KC, Borek DM, Wang T, et al. Structural and functional characterization of Reston Ebola VP35 Interferon Inhibitory Domain. J Mol Biol 2010.
[19] Haasnoot J, de Vries W, Geutjes EJ, Prins M, de Haan P, Berkhout B. The Ebola virus VP35 protein is a suppressor of RNA silencing. PLoS Pathog 2007;3:e86.
[20] Kimberlin CR, Bornholdt ZA, Li S, Woods Jr VL, MacRae IJ, Saphire EO. Ebolavirus VP35 uses a bimodal strategy to bind dsRNA for innate immune suppression. Proc Natl Acad Sci USA 2010;107:314–9.
[21] Bale S, Julien JP, Bornholdt ZA, Kimberlin CR, Halfmann P, Zandonatti MA, et al. Marburg virus VP35 can both fully coat the backbone and cap the ends of dsRNA for interferon antagonism. PLoS Pathog 2012;8:e1002916.
[22] Basler CF, Amarasinghe GK. Evasion of interferon responses by Ebola and Marburg viruses. J Interferon Cytokine Res 2009;29:511–20.
[23] Irwin JJ, Shoichet BK. ZINC—a free database of commercially available compounds for virtual screening. J Chem Inf Model 2005;45:177–82.
[24] Deng Z, Chuaqui C, Singh J. Structural interaction fingerprint (SIFt): a novel method for analyzing three-dimensional protein–ligand binding interactions. J Med Chem 2004;47:337–44.
[25] Laskowski RA, Swindells MB. LigPlot+: multiple ligand–protein interaction diagrams for drug discovery. J Chem Inf Model 2011;51:2778–86.
[26] Prins KC, Binning JM, Shabman RS, Leung DW, Amarasinghe GK, Basler CF. Basic residues within the ebolavirus VP35 protein are required for its viral polymerase cofactor function. J Virol 2010;84:10581–91.
[27] Towner JS, Paragas J, Dover JE, Gupta M, Goldsmith CS, Huggins JW, et al. Generation of eGFP expressing recombinant Zaire ebolavirus for analysis of early pathogenesis events and high-throughput antiviral drug screening. Virology 2005;332:20–7.
[28] Morris GM, Huey R, Lindstrom W, Sanner MF, Belew RK, Goodsell DS, et al. AutoDock4 and AutoDockTools4: automated docking with selective receptor flexibility. J Comput Chem 2009;30:2785–91.
[29] Jiang X, Kumar K, Hu X, Wallqvist A, Reifman J. DOVIS 2.0: an efficient and easy to use parallel virtual screening tool based on AutoDock 4.0. Chem Cent J 2008;2:18.
[30] Zhang S, Kumar K, Jiang X, Wallqvist A, Reifman J. DOVIS: an implementation for high-throughput virtual screening using AutoDock. BMC Bioinformatics 2008;9:126.
[31] Brooks BR, Brooks III CL, Mackerell Jr AD, Nilsson L, Petrella RJ, Roux B, et al. CHARMM: the biomolecular simulation program. J Comput Chem 2009;30:1545–614.
[32] Halgren TA. Merck molecular force field. I. Basis, form, scope, parameterization, and performance of MMFF94. J Comp Chem 1996;17:490–519.
[33] Krammer A, Kirchhoff PD, Jiang X, Venkatachalam CM, Waldman M. LigScore: a novel scoring function for predicting binding affinities. J Mol Graph Model 2005;23:395–407.
[34] Ramanan P, Edwards MR, Shabman RS, Leung DW, Endlich-Frazier AC, Borek DM, et al. Structural basis for Marburg virus VP35-mediated immune evasion mechanisms. Proc Natl Acad Sci USA 2012.
[35] Collaborative Computational Project, No. 4. The CCP4 suite: programs for protein crystallography. Acta Crystallogr 1994; D50:760–3.
[36] Adams PD, Afonine PV, Bunkoczi G, Chen VB, Davis IW, Echols N, et al. PHENIX: a comprehensive Python-based system for macromolecular structure solution. Acta Crystallogr D Biol Crystallogr 2010;66:213–21.
[37] Delaglio F, Grzesiek S, Vuister GW, Zhu G, Pfeifer J, Bax A. NMRPipe: a multidimensional spectral processing system based on UNIX pipes. J Biomol NMR 1995;6:277–93.
[38] Johnson BA. Using NMRView to visualize and analyze the NMR spectra of macromolecules. Methods Mol Biol 2004;278:313–52.
[39] Otwinowski Z, Minor W. Processing of X-ray diffraction data collected in oscilation mode. Methods Enzymol 1997;276:307–26.
[40] Emsley P, Cowtan K. Coot: model-building tools for molecular graphics. Acta Crystallogr D Biol Crystallogr 2004;60:2126–32.
[41] Davis IW, Leaver-Fay A, Chen VB, Block JN, Kapral GJ, Wang X, et al. MolProbity: all-atom contacts and structure validation for proteins and nucleic acids. Nucleic Acids Res 2007;35:W375–83.
[42] Muhlberger E, Weik M, Volchkov VE, Klenk HD, Becker S. Comparison of the transcription and replication strategies of marburg virus and Ebola virus by using artificial replication systems. J Virol 1999;73:2333–42.
[43] Luthra P, Ramanan P, Mire CE, Weisend C, Tsuda Y, Yen B, Liu G, Leung DW, Geisbert TW, Ebihara H, Amarasinghe GK, Basler CF. Mutual antagonism between the Ebola virus VP35 protein and the RIG-I activator PACT determines infection outcome. Cell Host Microbe 2013;14(1):74–84. http://dx.doi.org/10.1016/j.chom.2013.06.010.